Magnetic imaging of antiferromagnetic and superconducting phases in $Rb_xFe_{2-y}Se_2$ crystals

J. Hazi,[1] T. Mousavi,[1] P. Dudin,[2] G. van der Laan,[2] F. Maccherozzi,[2] A. Krzton-Maziopa,[3] E. Pomjakushina,[4] K. Conder,[4] and S. C. Speller[1,*]

[1]*Centre for Applied Superconductivity, Department of Materials, University of Oxford, Parks Road, Oxford OX1 3PH, United Kingdom*
[2]*Diamond Light Source, Harwell Science and Innovation Campus, Didcot OX11 0DE, United Kingdom*
[3]*Warsaw University of Technology, Faculty of Chemistry, Noakowskiego Street 3, PL-00-664 Warsaw, Poland*
[4]*Laboratory for Multiscale Materials Experiments, Paul Scherrer Institut, CH-5232 Villigen PSI, Switzerland*

(Received 29 November 2017; revised manuscript received 1 February 2018; published 15 February 2018)

High-temperature superconducting (HTS) cuprate materials, with the ability to carry large electrical currents with no resistance at easily reachable temperatures, have stimulated enormous scientific and industrial interest since their discovery in the 1980's. However, technological applications of these promising compounds have been limited by their chemical and microstructural complexity and the challenging processing strategies required for the exploitation of their extraordinary properties. The lack of theoretical understanding of the mechanism for superconductivity in these HTS materials has also hindered the search for new superconducting systems with enhanced performance. The unexpected discovery in 2008 of HTS iron-based compounds has provided an entirely new family of materials for studying the crucial interplay between superconductivity and magnetism in unconventional superconductors. Alkali-metal-doped iron selenide ($A_xFe_{2-y}Se_2$, A = alkali metal) compounds are of particular interest owing to the coexistence of superconductivity at relatively high temperatures with antiferromagnetism. Intrinsic phase separation on the mesoscopic scale is also known to occur in what were intended to be single crystals of these compounds, making it difficult to interpret bulk property measurements. Here, we use a combination of two advanced microscopy techniques to provide direct evidence of the magnetic properties of the individual phases. First, x-ray linear dichroism studies in a photoelectron emission microscope, and supporting multiplet calculations, indicate that the matrix (majority) phase is antiferromagnetic whereas the minority phase is nonmagnetic at room temperature. Second, cryogenic magnetic force microscopy demonstrates unambiguously that superconductivity occurs only in the minority phase. The correlation of these findings with previous microstructural studies and bulk measurements paves the way for understanding the intriguing electronic and magnetic properties of these compounds.

DOI: 10.1103/PhysRevB.97.054509

I. INTRODUCTION

The coexistence of superconductivity and antiferromagnetism has been observed in many iron-based compounds, and the intriguing balance between competing magnetic interactions is thought to be the key to understanding the origins of unconventional superconductivity. Alkali-metal-doped iron selenides ($A_xFe_{2-y}Se_2$, A = K, Cs, Rb) are an extreme example, exhibiting superconducting properties up to the relatively high temperature of about 30 K and, simultaneously, antiferromagnetic ordering that persists up to temperatures as high as 500 K [1,2]. Microstructural studies have revealed that superconducting single crystals of these compounds are intrinsically phase separated, with a striking microstructure consisting of a three-dimensional array of the minority phase in the form of plates aligned along the crystallographic {103} planes [3,4]. The minority phase is richer in Fe and deficient in Rb with respect to the matrix (majority phase) and has a tetragonal unit cell with a larger aspect (c/a) ratio. Bulk superconductivity (perfect magnetic shielding) and the ability to carry zero resistance transport currents have been observed in many single crystals of these compounds, but experiments such as muon spin rotation [5,6] and Mössbauer spectroscopy [7] find that a large volume fraction of these crystals (∼90%) also exhibit antiferromagnetic ordering. The accepted interpretation of these seemingly paradoxical results is that only the minority phase is superconducting, with a sufficient interconnection between the plates for macroscopic supercurrent transport enabling bulk shielding of the nonsuperconducting antiferromagnetic matrix. However, the microstructure does not appear to form a continuous network of the minority phase. Instead the mesoscale plate-shaped features appear to be broken into finer scale "platelets," again oriented along the {103} planes. Low-temperature microfocused x-ray diffraction (XRD) experiments by Ricci *et al.* have found that a third phase appears below about 300 K in $K_xFe_{2-y}Se_2$ crystals at the interfaces between the majority and minority phases, and they speculate that this additional phase provides a percolative superconducting pathway at low temperature [8]. In this paper, we study the spatial distribution at the relevant mesoscopic length scales of both the antiferromagnetically ordered phase at room temperature and the superconducting phase at 4.5 K in $Rb_xFe_{2-y}Se_2$ single crystals using two different advanced magnetic imaging probes.

Antiferromagnets are a notoriously difficult class of materials to study because the antiparallel alignment of magnetic

*susannah.speller@materials.ox.ac.uk

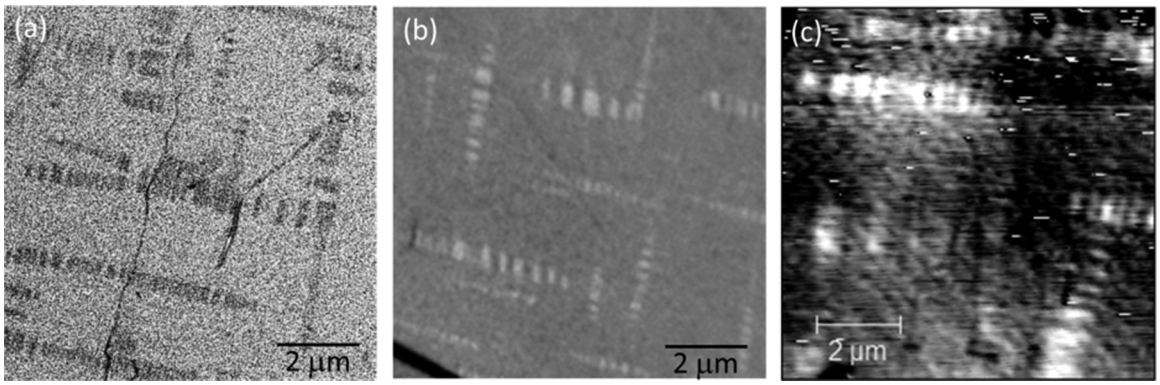

FIG. 1. Comparison between (a) backscattered electron image taken at room temperature in a SEM, mainly showing atomic number contrast, (b) polarization averaged PEEM image taken at room temperature, and (c) MFM image taken after cooling to 4.2 K in a field of 200 mT. The images are from different fragments of the same crystal. The same characteristic two-phase microstructure can be clearly observed in all of these images, which are shown with the same magnification.

moments results in a zero net macroscopic magnetization. Soft x-ray magnetic linear dichroism (XMLD) is increasingly being used as an element-specific probe for antiferromagnetic materials owing to the sensitivity of the absorption of linearly polarized x rays to the average value of the squared magnetic moment $\langle \mathbf{M}^2 \rangle$. From the XMLD signal, the difference in the absorption spectra from x rays polarized parallel and perpendicular to the magnetization direction, direct information can be extracted about the antiferromagnetism in the sample. This phenomenon has been modeled for various systems including the $M_{4,5}$ spectra of rare-earth elements [9] and the $L_{2,3}$ spectra of 3*d* transition-metal compounds [10] using atomic multiplet theory. The spectral line shape and the XMLD signal were initially found to depend on the relative orientation of the x-ray polarization direction and the spin axis [11]. However, it has been established that the orientation of the crystalline axes also strongly influences the spectra [12], hence allowing the determination of the crystallographic direction of the magnetic axis.

Photoelectron emission microscopy (PEEM) is a powerful technique for imaging the surface of magnetic materials. The sample is illuminated with monochromatic x rays and the emitted photoelectrons are collected with a series of lenses to generate an image of the photoelectron intensity. By varying the energy and polarization direction of the incident x rays, spatially resolved x-ray absorption spectroscopy (XAS) and XMLD studies can be performed. XMLD-PEEM has been widely used to image antiferromagnetic domains in thin films of various functional materials including NiO [11,13], $LaFeO_3$ [14], and $BaFeO_3$ [15], as well as more complex ferromagnetic/antiferromagnetic multilayered structures [16]. Recently, *in situ* XMLD-PEEM experiments have been performed, including investigating current-induced switching of antiferromagnetic domains in CuMnAs [17] and the effects of changing the ferroelectric polarization direction on antiferromagnetic domain structures in multiferroic $BiFeO_3$ [18,19].

In magnetic force microscopy (MFM), the local interactions between a sharp magnetic tip (mounted on a vibrating cantilever) and the stray magnetic field close to the sample are imaged by measuring small changes in the resonance of the cantilever. The spatial resolution of the MFM can be as good as 10 nm and is governed by the tip size and geometry as well as the distance between the tip and sample. This resolution surpasses all the common magnetic imaging techniques with the exception of electron microscopy, [20]. Its sensitivity ($\sim 10^{-4}\,\mathrm{T}/\sqrt{\mathrm{Hz}}$) is suitable for imaging individual superconducting flux quanta at low applied fields. However, its main strength lies in the ability to distinguish between topographic and magnetic signals by varying the lift-off distance. Low-temperature MFM has been used to study a wide range of superconductors including Nb [21,22], high-temperature superconducting (HTS) cuprate materials [21,23,24], and Fe-based materials [25], with the vast majority of the work involving studying vortex mechanics and vortex-vortex interactions in pristine materials.

II. EXPERIMENTAL DETAILS

The experiments reported here have all been carried out on fragments of the same $Rb_xFe_{2-y}Se_2$ crystal grown by the Bridgman technique detailed in Ref. [26], which has an onset T_c value of $\sim$29 K [27]. Figure 1 shows typical micrographs from freshly cleaved (001) surfaces, taken using the scanning electron microscope (SEM), PEEM, and MFM. The characteristic network of crystallographically aligned microstructural features, discussed in detail elsewhere [3,28], is visible in all of the images, enabling the minority and majority phases to be easily located in both the PEEM and MFM experiments. Since the material is highly air sensitive, the samples were stored in evacuated quartz tubes and freshly cleaved and mounted in an inert atmosphere glove box immediately prior to measurements to ensure that the data are representative of the bulk material. For the PEEM experiment, the cleaved crystal was fixed to the dedicated holder using conducting epoxy and cured on a hot plate in the glove box. A top post was also attached to the sample surface with conducting epoxy before transferring the sample in a sealed container to the PEEM instrument. The sample was cleaved in the load lock under flowing nitrogen by dislodging the top post immediately prior to evacuating the load lock to minimize exposure to air.

The PEEM images presented have been produced from the sum of a series of ten images taken at selected energies

around the Fe L_3 edge. In each case, the background has been removed using a standard procedure by dividing the image by an equivalent image taken at a photon energy far from the absorption peak. The absorption spectra have been normalized at the pre-edge. Polarization averaged images and spectra have been generated from the sum of the background corrected data taken with linear horizontal (LH) and linear vertical (LV) polarized x rays ($I_{\mathrm{LH}} + I_{\mathrm{LV}}$). Similarly, x-ray linear dichroism (XLD) images and spectra are produced from the difference in intensity of the background corrected LH and LV data ($I_{\mathrm{LH}} - I_{\mathrm{LV}}$).

In the multiplet modeling, the wave functions of the ground and final states were calculated in intermediate coupling using Cowan's Hartree-Fock code with a relativistic correction [10]. The Slater and spin-orbit parameters are as tabulated in Ref. [29]. Interatomic screening and mixing was taken into account by reducing the atomic values of the Slater integrals $F_k(3d, 3d)$, $F_k(2p, 3d)$, and $G_k(2p, 3d)$ to 70%. For the tetrahedral Fe site a crystal field strength of $10Dq = 1.5\,\mathrm{eV}$ and an exchange field of $g\mu_{\mathrm{B}}H = 10\,\mathrm{meV}$ were used to fit the spectra. The calculated results were broadened by a Lorentzian with a half width at half maximum (HWHM) of $\Gamma = 0.15$ (0.4) eV for the L_3 (L_2) edge to account for intrinsic linewidth broadening and a Gaussian with a standard deviation of $\sigma = 0.25\,\mathrm{eV}$ for the instrumental broadening.

Magnetic force microscopy was performed in an AttoDRY1000 cryostat equipped with a 9 T/3 T superconducting vector magnet using an Attocube MFM-1 microscope with a Point Probe® Plus Magnetic Force Microscopy–Reflex (PPP-MFMR) tip. The transfer time during which the surface was exposed to air was estimated to be less than 1 min. The sample space was evacuated to a base pressure of 10^{-4} mbar, and backfilled with 30 mbar of He gas. The experimental procedure for obtaining each MFM image involved the following steps. First, the desired temperature and background field were set. The resonant frequency of the tip at the starting position of the scan (bottom left corner of the image) was measured with the tip roughly 10 μm above the surface. The tip was then set to oscillate at its resonant frequency and was brought into contact with the surface before being lifted off by a set distance of 150 nm. The oscillation frequency was retuned to the resonant frequency at this imaging distance.

III. PEEM STUDY

To investigate the spatial distribution of the antiferromagnetic phase in single crystals of $Rb_xFe_{2-y}Se_2$, XLD experiments have been performed using the PEEM instrument on beamline I06 at the Diamond Light Source. The schematic diagram in Fig. 2 shows the experimental setup. X rays are incident on the sample at a fixed angle of $\alpha = 16^\circ$. The electric field component **E** of the incident x rays is oriented in the plane of the sample for linear horizontal (LH) polarization and almost parallel to the sample normal (crystallographic [001] direction) for linear vertical (LV) polarization.

Figures 3(a) and 3(b) show PEEM images taken at the Fe L_3 edge, clearly revealing the well-known two-phase microstructure. Terrace edges are also visible as dark lines across the images. In the polarization averaged image [Fig. 3(a)], the minority phase is brighter in contrast to the matrix, indicating

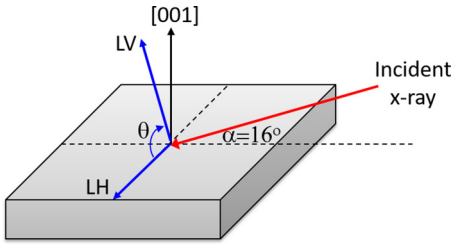

FIG. 2. Schematic diagram showing the experimental geometries with LH and LV in the PEEM.

the concentration of Fe is higher in this phase. This is consistent with the SEM/energy-dispersive x-ray spectroscopy (EDX) chemical analysis reported previously [3].

Using the PEEM images to locate suitable regions of interest, absorption spectra for the different phases have been obtained. Figure 3(c) shows polarization averaged Fe $L_{2,3}$-edge XAS from the matrix and minority phases. Since the $L_{2,3}$ absorption spectrum results from the excitation of electrons from the core Fe $2p$ levels to unoccupied $3d$ states, these spectra are sensitive to the local bonding environment of Fe. The core-hole spin-orbit interaction leads to splitting of the final state into two manifolds corresponding to $j = \frac{3}{2}$ and $\frac{1}{2}$, which are well separated in energy, resulting in the L_3 and L_2 structures at 707 and 720 eV, respectively. The branching ratio $\frac{I(L_3)}{I(L_3)+I(L_2)}$ is the fraction of the integrated intensity of the $L_{2,3}$ spectrum that results from transitions from the $2p_{3/2}$ core level [30,31]. In the matrix and minority phase spectra, the measured branching ratio is close to 0.77. This is considerably higher than the statistical value of 0.667 expected for a degenerate initial state. This high branching ratio is characteristic of Fe compounds in a high spin configuration [31], and is consistent with the large magnetic moment of up to 3.3 μ_{B} per Fe atom found in the antiferromagnetic phase of $A_xFe_{2-x}Se_2$ by neutron diffraction experiments [32–34]. The spectral shape is similar to metallic Fe alloys and covalent compounds, lacking the fine multiplet structure that is observed for ionic Fe oxides and other ionic compounds [30]. Similar spectra have been reported for other Fe-based superconductors [35,36] and related compounds, e.g., FeS [37], and the spectral shape has been attributed to short Fe-Fe bond lengths resulting in strong delocalization of the Fe $3d$ electrons. The narrow single L_3 peak indicates that no discernible oxidation of the $Rb_xFe_{2-y}Se_2$ surface has occurred, as confirmed by O K-edge XAS [27]. The spectra were reconstructed from carefully selected regions of the image, but owing to the small length scale, the minority phase region is likely to include a small contribution from the matrix. Both spectra have very similar line shapes and peak widths, indicating that the local Fe bonding environment is similar in the two phases.

Figure 3(d) shows the Fe $2p$ x-ray photoemission spectrum (XPS) from a clean surface of a similar crystal, prepared by cleaving in UHV. The peak positions are again consistent with Fe being in the metallic state, with the presence of a broad, weak satellite structure at higher energy of around 730 eV (indicated by the arrow). This satellite feature has been observed previously in FeS and Fe_7Se_8, and Shimada *et al.* propose that it is a plasmon loss peak associated with Fe $2p_{3/2}$ rather than originating from charge-transfer effects

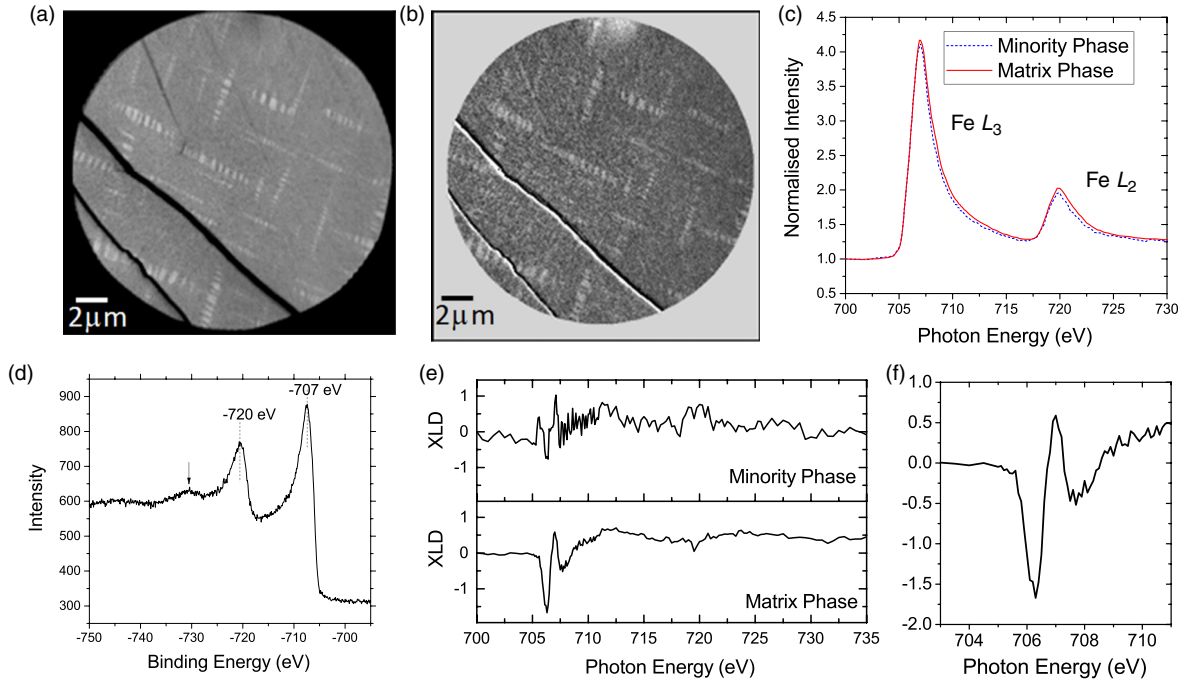

FIG. 3. PEEM images taken at a photon energy of 706.1 eV showing (a) polarization averaged intensity (LH + LV) and (b) x-ray linear dichroism signal (LH-LV). (c) Polarization averaged (LH + LV) Fe $L_{2,3}$ XAS from the matrix and minority phases. (d) XPS spectrum of the Fe $2p$ peaks on a different sample taken on the Antares beamline at Soleil Synchrotron. The arrow indicates the presence of a satellite peak. (e) Comparison of the XLD spectra for the minority and matrix phases. (f) Detailed view of the XLD signal observed at the L_3 edge in the matrix phase.

characteristic of localized Fe $3d$ electrons [38]. However, it is worth noting that this satellite feature is not observed in Fe metal or superconducting LaFeAsO, providing evidence that the Fe $3d$ electrons are itinerant in these materials [39].

Typical XLD spectra from the matrix and minority phases are shown in Figs. 3(e) and 3(f). In the matrix, the spectra reproducibly show a feature with a dip (706.2 eV), followed by a peak (707 eV) at the Fe L_3 edge. There is also a weak feature discernible at the L_2 edge. These features are absent in XLD spectra from the minority phase. The XLD image in Fig. 3(b) is taken at a photon energy of 706.1 eV, close to the minimum in the XLD spectrum of the matrix. The minority phase has a similar contrast to the background (zero dichroism), whereas the matrix phase is darker (negative dichroic signal) at this photon energy.

IV. MULTIPLET CALCULATIONS

The Fe $L_{2,3}$ XAS have been calculated from the electric-dipole-allowed transitions between the crystal-field ground-state Fe^{2+} $3d^6$ and the final-state $2p^5 3d^7$ configurations. The spectra depend on the orientation of the magnetic field vector **H** and the x-ray polarization vector **E** with respect to the crystalline axes. When the point-group symmetry of the excited

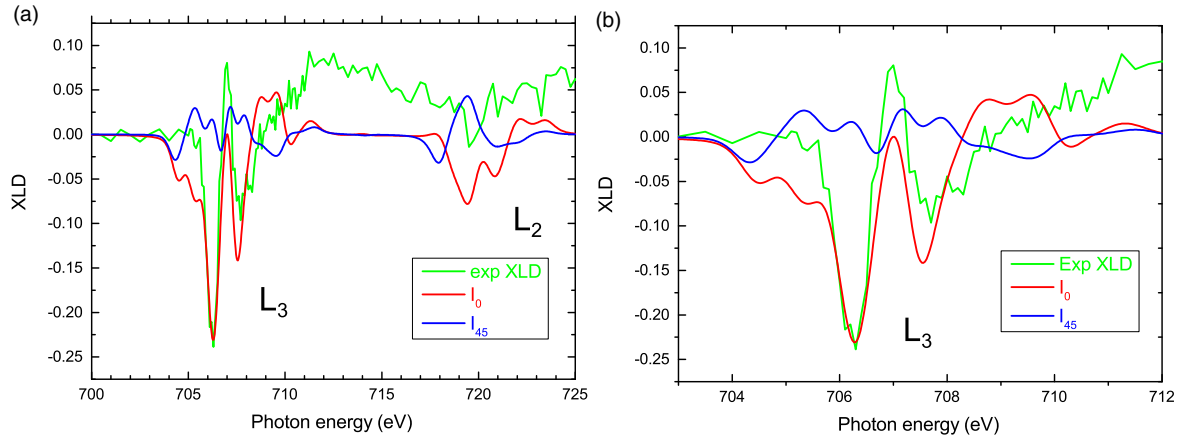

FIG. 4. Experimental spectrum for the matrix phase (green curve) compared to the calculated XLD spectra, I_0 and I_{45} (red and blue curve, respectively), obtained from multiplet calculations (a) for the Fe $L_{2,3}$ edge and (b) the L_3 edge shown on an expanded scale.

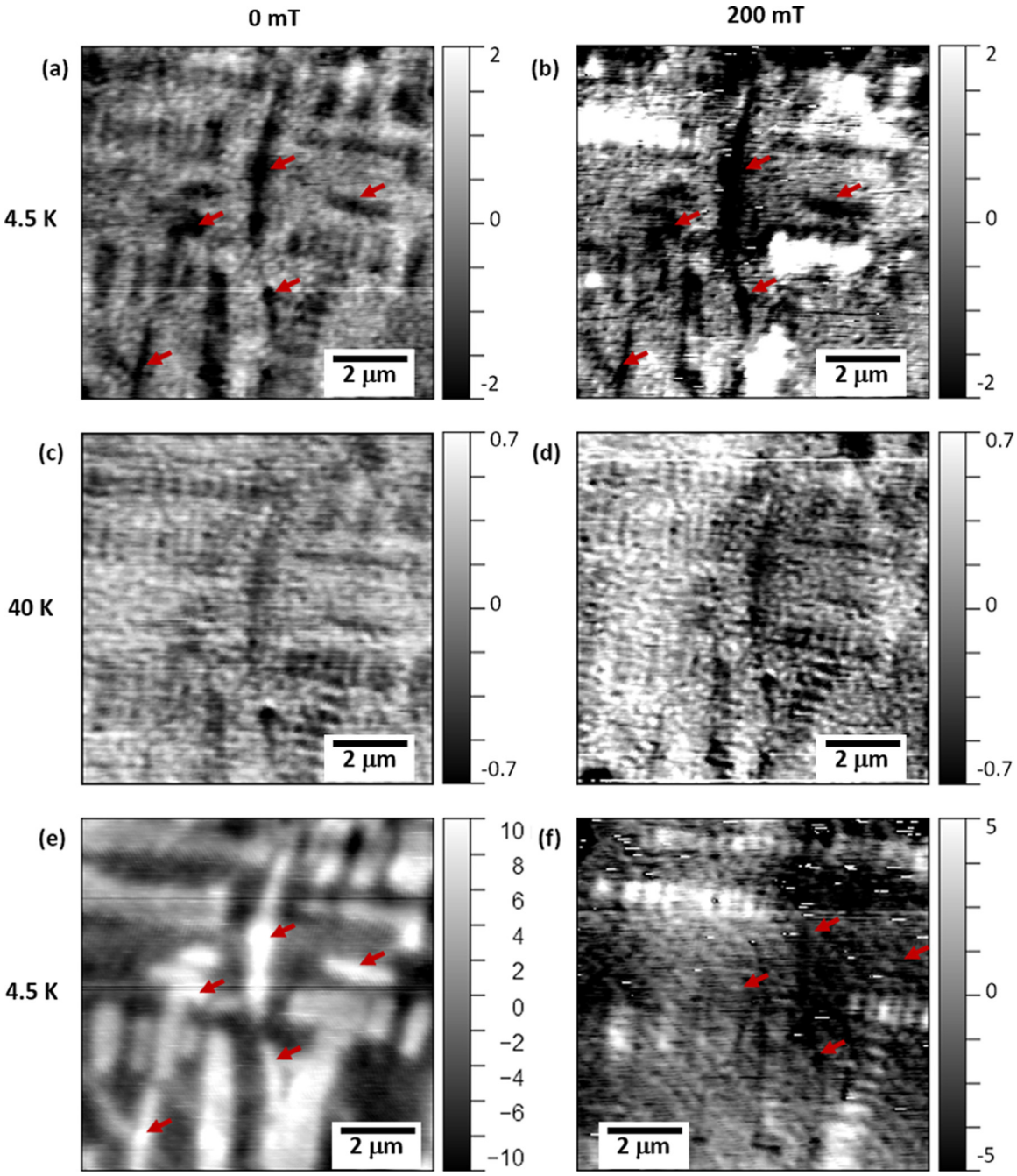

FIG. 5. Constant height MFM images taken from the same area of the sample at (a) 4.5 K, 0 T, (b) 4.5 K, 200 mT, (c) 40 K, 0 mT, and (d) 40 K, 200 mT. Note the image contrast scales are not the same in each image. (e) Image taken in phase-locked-loop constant force mode with a bias voltage of 5 V applied to the tip. (f) Constant height image taken after field cooling in 200 mT to 4.5 K.

atom is approximately cubic, there are two independent XMLD spectra, I_0 and I_{45}, with different energy dependences, defined in Refs. [12,40] as

$$I_0 = I(E_{[100]}, H_{[100]}) - I(E_{[010]}, H_{[100]}), \quad (1)$$

$$I_{45} = I(E_{[110]}, H_{[110]}) - I(E_{[1\bar{1}0]}, H_{[110]}). \quad (2)$$

The calculated I_0 and I_{45} spectra are shown in Fig. 4. The photon energy scale was fixed by setting the L_3 peak maximum of the calculated total XAS to that of the experiment. Figure 4 shows that there is a good agreement between the experimental XMLD (green curve) and calculated I_0 spectrum (red curve), particularly at the L_3 edge.

Considering the geometry of the XLD-PEEM experiment (shown in Fig. 2) and assuming that the spin axis is along the crystallographic [001] axis [34], the XMLD signal is given by

$$\begin{aligned} \text{XMLD} &= \text{XAS}(90-\theta) - \text{XAS}(\text{LV}) \\ &= \sin^2(90-\theta)(0.82I_0 + 0.18I_{45}), \end{aligned} \quad (3)$$

where $\theta = 0^\circ$ corresponds to LH, and $\theta = 90^\circ$ corresponds to LV. Therefore, it is expected that the experimental XLD

spectrum is largely dominated by I_0, as observed here. The small contribution from I_{45} arises because the incident x rays are not fully at grazing incidence but make a small angle of 16° with the sample surface in the PEEM experimental geometry (see Fig. 2). The good agreement between the calculated XMLD spectrum and the experimental data strongly suggests that the linear dichroism in the matrix is due to antiferromagnetic ordering with spins aligned along [001].

V. MFM STUDY

Cryogenic magnetic force microscopy (MFM) has been used to probe local variations in magnetic field in the vicinity of the sample by scanning a vibrating magnetic tip above the surface in constant height mode. In our experiments, increasing the strength of the applied magnetic field was found to produce a shift in the resonant frequency of the tip towards lower values, leading to a negative phase shift for a tip oscillating at a fixed frequency [27]. The MFM images shown here are taken using a fixed tip frequency and phase shift ($\Delta\phi$) as the measured signal. Therefore, bright regions (positive phase shift) correspond to regions of lower magnetic field. Superconducting features are expected to appear bright when a background field is applied owing to flux expulsion.

MFM images have been taken by cooling to 4.5 K in zero applied field [zero-field-cooling (ZFC) mode] and subsequently applying a magnetic field of 200 mT in a direction perpendicular to the surface of the sample (i.e., parallel to the *c* axis of the crystal). Figure 5(a), taken in zero background field, is essentially a topographic image of the surface. The familiar phase-separated microstructure can clearly be seen, with the minority phase appearing darker than the matrix. In addition, the surface seems to be covered in small particles about 50 nm in size. These may be oxide particles resulting from the surface being briefly exposed to air during loading of the sample, and are often also seen in SEM images [27]. On applying a magnetic field of 200 mT, bright features appear in the image [Fig. 5(b)]. Comparing with the topographic image in Fig. 5(a), it can be seen that these occur in locations where the characteristic stripy morphology of the minority phase can be seen. Since bright features represent a lower magnetic field, this strongly suggests that the minority phase features demonstrate bulk superconductivity because magnetic flux is being expelled from their interior. To confirm that this magnetic contrast is associated with superconductivity, the measurements were repeated above T_c (40 K). By comparing Figs. 5(b) and 5(d), it is clear that the bright features seen at 4.5 K do not appear above T_c. This provides convincing evidence of the existence of superconductivity in the minority phase.

It is worth noting that not all of the features that appear dark in the topographic image of Fig. 5(a) seem to be superconducting, as indicated by red arrows. To investigate this further, different imaging modes and cooling protocols have been used. Figure 5(e) shows an image taken in zero magnetic field with a bias voltage applied to the tip. Under these imaging conditions the microscope is effectively probing the contact potential difference, with the contrast mainly due to changes in the electrostatic interaction between the tip and the sample. In this image, all of the dark topographic features appear bright relative to the matrix, suggesting that, regardless of whether the features exhibit superconductivity, they are electronically similar. In addition, Fig. 5(f) shows an MFM scan taken after field cooling at 200 mT from above T_c to 4.5 K. The same features appear bright as in the image taken using the zero-field-cooling protocol, confirming that only some of the features in this sample exhibit superconductivity at 4.5 K. The stripy nature of the minority phase is clearly visible in this image. However, in the electrical image [Fig. 5(e)], the features appear to be more continuous, suggesting that the regions between the secondary phase stripes may be electrically conducting but not superconducting (or only weakly superconducting) at 4.5 K. This may be linked to the presence of an interface phase found to appear in $K_xFe_{2-y}Se_2$ crystals below room temperature in the microfocused XRD results of Ricci *et al.* [8]. However, further experiments at temperatures between 100 and 300 K are required to obtain conclusive results.

VI. CONCLUSIONS

We have reported the results of two separate experiments using spatially resolved probes to study the magnetic properties of the individual phases in $Rb_xFe_{2-y}Se_2$ crystals. As illustrated in Fig. 1, the characteristic phase-separated microstructure observed in the SEM is also clear in the PEEM and MFM images, making it easy to directly compare the results from the different experiments. The XLD-PEEM study, carried out at room temperature, strongly suggests that the matrix phase is antiferromagnetically ordered, whereas the minority phase is nonmagnetic. Theoretical calculations and neutron diffraction studies reviewed by Mou *et al.* [2] have found that the Fe-vacancy-ordered "245" phase is a block antiferromagnet with its magnetic moments aligned along the crystallographic [001] axis, whereas the Fe-vacancy-free phase is paramagnetic in nature at room temperature. Therefore this XLD-PEEM study provides direct evidence that the matrix is the antiferromagnetic Fe-deficient 245 phase. This is consistent with a previous chemical composition analysis that found the matrix to have a chemical composition close to the 245 stoichiometry of the Fe-vacancy-ordered phase [3]. The minority phase is richer in Fe, as expected for the paramagnetic Fe-vacancy-free phase. The results are also consistent with previous muon spin rotation experiments which found that around 90% by volume of these crystals is antiferromagnetic, with the remaining 10% being paramagnetic at room temperature [5]. Since linear dichroic signals can also arise from an anisotropic charge distribution in a material, these PEEM experiments at a single temperature with no external magnetic field do not prove absolutely that the origin of the linear dichroism is antiferromagnetic ordering. However, the close similarity of the experimental data with the XMLD calculations provides additional weight to this argument. The cryogenic MFM study has clearly shown that superconductivity is only present in the minority phase.

The combination of these two unique experiments gives strong evidence that the minority phase is paramagnetic at room temperature and becomes superconducting on cooling below 30 K. By contrast, the matrix is antiferromagnetic and nonsuperconducting. This study has demonstrated that both XLD-PEEM and cryogenic MFM are powerful techniques for understanding the local magnetic properties of inhomogeneous superconductors.

ACKNOWLEDGMENTS

J.H. acknowledges support in the form of a Doctoral Training Account studentship (EP/M508111/1) from the U.K. Engineering and Physical Sciences Research Council. T.M. is grateful for support from the Oxfordshire Local Enterprise Partnership as part of the Oxford Centre for Applied Superconductivity. We thank Tim Davies for superconducting quantum interference device (SQUID) magnetometry and Diamond Light Source for access to beamline I06 (si10251-1) that contributed to the results presented here.

Data in support of this paper is available at the Oxford Research Archive [41].

[1] A. Krzton-Maziopa, Superconductivity in alkali metal intercalated iron selenides, J. Phys.: Condens. Matter **28**, 293002 (2016).

[2] D.-X. Mou, L. Zhao, and X.-J. Zhou, Structural, magnetic and elecronic properties of the iron-chalcogenide $A_xFe_{2-y}Se_2$ (A = K, Cs, Rb, and Tl, etc.), Front. Phys. **6**, 410 (2011).

[3] S. C. Speller, P. Dudin, S. Fitzgerald, G. M. Hughes, K. Kruska, T. B. Britton, A. Krzton-Maziopa, E. Pomjakushina, K. Conder, A. Barinov, and C. R. M. Grovenor, High-resolution characterization of microstructural evolution in $Rb_xFe_{2-y}Se_2$ crystals on annealing, Phys. Rev. B **90**, 024520 (2014).

[4] Z. Wang, Y. Cai, Z. W. Wang, C. Ma, Z. Chen, H. X. Yang, H. F. Tian, and J. Q. Li, Archimedean solidlike superconducting framework in phase-separated $K_{0.8}Fe_{1.6+x}Se_2$ ($0 < x < 0.15$), Phys. Rev. B **91**, 064513 (2015).

[5] Z. Shermadini, H. Luetkens, R. Khasanov, A. Krzton-Maziopa, K. Conder, E. Pomjakushina, H.-H. Klauss, and A. Amato, Superconducting properties of single-crystalline $A_xFe_{2-y}Se_2$ (A = Rb, K) studied using muon spin spectroscopy, Phys. Rev. B **85**, 100501(R) (2012).

[6] C. N. Wang, P. Marsik, R. Schuster, A. Dubroka, M. Rossle, C. Niedermayer, G. D. Varma, A. F. Wang, X. H. Chen, T. Wolf, and C. Bernhard, Macroscopic phase segregation in superconducting $K_{0.73}Fe_{1.67}Se_2$ as seen by muon spin rotation and infrared spectroscopy, Phys. Rev. B **85**, 214503 (2013).

[7] D. H. Ryan, W. N. Rowan-Weetaluktuk, J. M. Cadogan, R. Hu, W. E. Straszheim, S. L. Bud'ko, and P. C. Canfield, ^{57}Fe Mossbauer study of magnetic ordering in superconducting $K_{0.80}Fe_{1.76}Se_{2.00}$ single crystals, Phys. Rev. B **83**, 104526 (2011).

[8] A. Ricci, N. Poccia, B. Joseph, D. Innocenti, G. Campi, A. Zozulya, F. Westermeier, A. Schavkan, F. Coneri, A. Bianconi, H. Takeya, Y. Mizuguchi, Y. Takano, T. Mizokawa, M. Sprung, and N. L. Saini, Direct observation of nanoscale interface phase in the superconducting chalcogenide $K_xFe_{2-y}Se_2$ with intrinsic phase separation, Phys. Rev. B **91**, 020503 (2015).

[9] B. T. Thole, G. van der Laan, and G. A. Sawatzky, Strong Magnetic Dichroism Predicted in the $M_{4,5}$ X-Ray Absorption Spectra of Magnetic Rare Earth Elements, Phys. Rev. Lett. **55**, 2086 (1985).

[10] G. van der Laan and B. T. Thole, Strong magnetic x-ray dichroism in $2p$ absorption spectra of $3d$ transition-metal ions, Phys. Rev. B **43**, 13401 (1991).

[11] D. Alders, L. H. Tjeng, F. C. Voogt, T. Hibma, G. A. Sawatzky, C. T. Chen, J. Vogel, M. Sacchi, and S. Iacobucci, Temperature and thickness dependence of magnetic moments in NiO epitaxial films, Phys. Rev. B **57**, 11623 (1998).

[12] G. van der Laan, E. Arenholz, R. V. Chopdekar, and Y. Suzuki, Influence of crystal field on anisotropic x-ray magnetic linear dichroism at the Co^{2+} $L_{2,3}$ edges, Phys. Rev. B **77**, 064407 (2008).

[13] H. Ohldag, G. van der Laan, and E. Arenholz, Correlation of crystallographic and magnetic domains at Co/NiO(001) interfaces, Phys. Rev. B **79**, 052403 (2009).

[14] A. Scholl, J. Stohr, J. Luning, J. W. Seo, J. Fompeyrine, H. Siegwart, J.-P. Locquet, F. Nolting, S. Anders, E. E. Fullerton, M. R. Scheinfein, and H. A. Padmore, Observation of antioferromagnetic domains in epitaxial thin films, Science **287**, 1014 (2000).

[15] M. B. Holcomb, L. W. Martin, A. Scholl, Q. He, P. Yu, C.-H. Yang, S. Y. Yang, P.-A. Glans, M. Valvidares, M. Huijben, J. B. Kortright, J. Guo, Y. H. Chu, and R. Ramesh, Probing the evolution of antiferromagnetism in multiferroics, Phys. Rev. B **81**, 134406 (2010).

[16] J. Wu, D. Carlton, J. S. Park, Y. Meng, E. Arenholz, A. Doran, A. T. Young, A. Scholl, C. Hwang, H. W. Zhao, J. Bokor, and Z. Q. Qiu, Direct observation of imprinted antiferromagnetic vortex states in CoO/Fe/Ag(001) discs, Nat. Phys. **7**, 303 (2011).

[17] M. J. Grzybowski, P. Wadley, K. W. Edmonds, R. Beardsley, V. Hills, R. P. Campion, B. L. Gallagher, J. S. Chauhan, V. Novak, T. Jungwirth, F. Maccherozzi, and S. S. Dhesi, Imaging Current-Induced Switching of Antiferromagnetic Domains in CuMnAs, Phys. Rev. Lett. **118**, 057701 (2017).

[18] W. Saenrang, B. Davidson, F. Maccherozzi, J. Podkaminer, J. Irwin, R. Johnson, J. Freeland, J. Iniguez, J. Schad, K. Reierson, J. Frederick, C. Vaz, L. Howald, T.-H. Kim, S. Ryu, M. van Veenendaal, P. Radaelli, S. Dhesi, M. Rzchowski, and C. B. Eom, Deterministic and robust room-temperature exchange coupling in monodomain multiferroic $BiFeO_3$ heterostructures, Nat. Commun. **8**, 1583 (2017).

[19] T. Zhao, A. Scholl, F. Zavaliche, K. Lee, M. Barry, A. Doran, M. P. Cruz, Y. H. Chu, C. Ederer, N. A. Spaldin, R. R. Das, D. M. Kim, S. H. Baek, C. B. Eom, and R. Ramesh, Electrical control of antiferromagnetic domains in multiferroic $BiFeO_3$ films at room temperature, Nat. Mater. **5**, 823 (2006).

[20] J. R. Kirtley, Fundamental studies of superconductors using scanning magnetic imaging, Rep. Prog. Phys. **73**, 126501 (2010).

[21] A. Volodin, K. Temst, Y. Bruynseraede, C. Van Haesendonck, M. I. Montero, I. K. Schuller, B. Dam, J. M. Huijbregtse, and R. Griessen, Magnetic force microscopy of vortex pinning at grain boundaries in superconducting thin films, Physica C: Superconduc. **369**, 165 (2002).

[22] F. Bobba, C. Di Giorgio, A. Scarfato, M. Longobardi, M. Iavarone, S. A. Moore, G. Karapetrov, V. Novosad, V. Yefremenko, and A. M. Cucolo, Vortex-antivortex coexistence in Nb-based superconductor/ferromagnet heterostructures, Phys. Rev. B **89**, 214502 (2014).

[23] H. J. Hug, A. Moser, I. Parashikov, B. Stiefel, O. Fritz, H.-J. Guntherodt, and H. Thomas, Observation and manipulation of vortices in a $YBa_2Cu_3O_7$ thin film with a low temperature magnetic force microscope, Physica C: Superconduc. **235–240**, 2695 (1994).

[24] O. M. Auslaender, L. Luan, E. W. J. Straver, J. E. Hoffman, N. C. Koshnick, E. Zeldov, D. A. Bonn, R. Liang, W. N. Hardy, and K. A. Moler, Mechanics of individual isolated vortices in a cuprate superconductor, Nat. Phys. **5**, 35 (2008).

[25] Y. Lamhot, A. Yagil, N. Shapira, S. Kasahara, T. Watashige, T. Shibauchi, Y. Matsuda, and O. M. Auslaender, Local characterisation of superconductivity in $BaFe_2(As_{1-x}P_x)_2$, Phys. Rev. B **91**, 060504(R) (2015).

[26] A. Krzton-Maziopa, E. Pomjakushina, and K. Conder, Single crystals of novel alkali metal intercalated iron chalcogenide superconductors, J. Cryst. Growth **360**, 155 (2012).

[27] See Supplemental Material at http://link.aps.org/supplemental/10.1103/PhysRevB.97.054509 for more details of $Rb_xFe_{2-y}Se_2$ crystal quality and additional supporting PEEM and MFM results.

[28] S. C. Speller, T. B. Britton, G. M. Hughes, A. Krzton-Maziopa, E. Pomjakushina, K. Conder, A. T. Boothroyd, and C. R. M. Grovenor, Microstructural analysis of phase separation in iron chalcogenide superconductors, Supercond. Sci. Technol. **25**, 084023 (2012).

[29] G. van der Laan and I. W. Kirkman, The $2p$ absorption spectra of $3d$ transition metal compounds in tetrahedral and octahedral symmetry, J. Phys.: Condens. Matter **4**, 4189 (1992).

[30] P. S. Miedema and F. M. F. de Groot, The iron L edges: Fe $2p$ x-ray absorption and electron energy loss spectroscopy, J. Electron Spectrosc. Relat. Phenom. **187**, 32 (2013).

[31] B. T. Thole and G. van der Laan, Branching ratio in x-ray absorption spectroscopy, Phys. Rev. B **38**, 3158 (1988).

[32] V. Y. Pomjakushin, D. V. Sheptyakov, E. Pomjakushina, A. Krzton-Maziopa, K. Conder, D. Chernyshov, V. Svitlyk, and Z. Shermadini, Iron-vacancy superstructure and possible room-temperature antiferromagnetic order in superconducting $Cs_yFe_{2-x}Se_2$, Phys. Rev. B **83**, 144410 (2011).

[33] V. Y. Pomjakushin, E. Pomjakushina, A. Krzton-Maziopa, K. Conder, and Z. Shermadini, Room temperature antiferromagnetic order in superconducting $X_yFe_{2-x}Se_2$ (X = Rb, K): A neutron powder diffraction study, J. Phys.: Condens. Matter **23**, 156003 (2011).

[34] M. Wang, M. Wang, G. N. Li, Q. Huang, C. H. Li, G. T. Tan, C. L. Zhang, H. Cao, W. Tian, Y. Zhao, Y. C. Chen, X. Y. Lu, B. Sheng, H. Q. Luo, S. L. Li, M. H. Fang, J. L. Zarestky, W. Ratcliff, M. D. Lumsden, J. W. Lynn, and P. Dai, Antiferromagnetic order and superlattie structure in nonsuperconducting and superconducting $Rb_yFe_{1.6+x}Se_2$, Phys. Rev. B **84**, 094504 (2011).

[35] F. Bondino, E. Mangnano, C. H. Booth, F. Offi, G. Panaccione, M. Malvestuto, G. Paolicelli, L. Simonelli, F. Parmigiani, M. A. McGuire, A. S. Sefat, B. C. Sales, R. Jin, P. Vilmercati, D. Mandrus, D. J. Singh, and N. Manella, Electronic structure of $CeFeAsO_{1-x}F_x$ ($x = 0, 0.11,$ and 0.12), Phys. Rev. B **82**, 014529 (2010).

[36] T. Kroll, S. Bonhommeau, T. Kachel, H. A. Durr, J. Werner, G. Behr, A. Koitzsch, R. Hubel, S. Leger, R. Schonfelder, A. K. Ariffin, R. Manzke, F. M. F. De Groot, J. Fink, H. Eschrig, B. Buchner, and M. Knupfer, Electronic structure of $LaFeAsO_{1-x}F_x$ from x-ray absorption spectroscopy, Phys. Rev. B **78**, 220502(R) (2008).

[37] K. D. Kwon, K. Refson, S. Bone, R. Qiao, W.-L. Yang, Z. Liu, and G. Sposito, Magnetic ordering in tetragonal FeS: Evidence for strong itinerant spin fluctuations, Phys. Rev. B **83**, 064402 (2011).

[38] K. Shimada, T. Mizokawa, K. Mamiya, T. Saitoh, A. Fujimori, K. Ono, A. Kakizaki, T. Ishii, M. Shirai, and T. Kamimura, Spin-integrated and spin-resolved photoemission study of Fe chalcogenides, Phys. Rev. B **57**, 8845 (1998).

[39] W. Malaeb, T. Yoshida, T. Kataoka, A. Fujimori, M. Kubota, K. Ono, H. Usui, K. Kuroki, R. Arita, H. Aoki, Y. Kamihara, M. Hirano, and H. Hosono, Electronic structure and electron correlation in $LaFeAsO_{1-x}F_x$ and $LaFePO_{1-x}F_x$, J. Phys. Soc. Jpn. **77**, 093714 (2008).

[40] E. Arenholz, G. van der Laan, R. V. Chopdekar, and Y. Suzuki, Anisotropic x-ray magnetic linear dichroism at the $Fe_{2,3}$ edges in Fe_3O_4, Phys. Rev. B **74**, 094407 (2006).

[41] www.ora.ox.ac.uk